Journal of Materials Chemistry A

ROYAL SOCIETY OF CHEMISTRY

PAPER

View Article Online
View Journal

Cite this: DOI: 10.1039/d6ta01363e

Structure–property–performance relationship of a series of CO_2RR-active N-doped mesoporous carbon frameworks

Jialang Li, [a] Ahmed Ali,[ab] Linke Huang,[c] Ruohong Sui, [a] Robert Marriott,[a] Chandra Singh [c] and Viola Birss *[a]

While electrochemical CO_2 reduction (CO_2RR) enables the sustainable conversion of CO_2 to value-added products, the design of efficient, selective, and earth-abundant catalysts remains challenging. Metal catalysts, commonly used for aqueous CO_2RR, can exhibit limited selectivity, instability, and high cost, thus hindering large-scale implementation. In contrast, heteroatom-doped (*e.g.*, nitrogen) carbons that selectively convert CO_2 to CO are emerging as possible alternatives. However, the relationship between the nitrogen content and functionalities, the carbon support properties, and the CO_2RR performance, remains unclear, due in large part to the significant variations in the carbon materials employed to date. To address this, we systematically investigated a series of ordered, silica colloid-imprinted mesoporous carbon powders with highly reproducible and tunable pore sizes, known nitrogen speciation, and varying degrees of carbon crystallinity on the CO_2RR selectivity and activity. The results show that CO selectivity is mainly governed by the presence of structural disorder in the carbon framework as well as by a rich density of pyridinic nitrogen surface sites, with the best performing N-C catalyst exhibiting an exceptional CO faradaic efficiency of 97%. DFT calculations were also conducted, confirming that pyridinic-N sites offer the most favourable binding for CO_2 intermediates during CO production, supporting the superior CO_2RR activity observed experimentally. It is also shown that the CO_2RR activity correlates with nitrogen content and accessible surface area, showing an onset overpotential of only −240 mV. These insights reveal some key structure–property–performance relationships that govern CO_2 reduction at N-doped carbons, offering guidance especially for the design and preparation of new carbon supports with optimal properties.

Received 12th February 2026
Accepted 16th April 2026

DOI: 10.1039/d6ta01363e

rsc.li/materials-a

Introduction

The atmospheric concentration of carbon dioxide (CO_2), a well-known greenhouse gas, reached 420 ppm in 2024 primarily due to excessive fossil fuel consumption, leading to accelerated global warming. Renewable energy is an alternative energy source that generates few emissions, but its intermittent nature limits a consistent global supply, necessitating efficient energy storage technologies.[1] One solution is electrochemical CO_2 reduction (CO_2RR), which stores electricity in the form of fuels and chemicals by the conversion of CO_2 to CO, ethylene, ethanol, methanol, and even methane, thus potentially replacing fossil fuels.[2]

While CO_2RR can be accomplished at metal or metal oxide catalysts in high-temperature all-solid-state devices (solid oxide electrolysis cells) at high efficiencies, various challenges, arising from a range of degradation processes, are still a problem.[3,4] In aqueous room-temperature CO_2RR systems, metal-based catalysts, such as Cu, Au, Ag, and Zn, are the most common, but these systems are plagued by sluggish kinetics, poor selectivity, and durability issues exacerbated by morphological instability, which together result in high cost.[5] Therefore, the search is on for other CO_2RR catalysts that could replace bulk metals.

One option is carbon-based materials, as carbon is abundant, cost-effective, environmentally friendly, and can be produced at large scale. However, pristine carbons are completely inactive towards the CO_2RR and therefore must be altered, *e.g.*, by surface modification with CO_2-reducing molecular catalysts,[6,7] or by doping with heteroatoms.[1,8–10] For example, doping with nitrogen, which is an abundant low-cost element, is a highly promising method for modifying the surface of carbon materials to make them CO_2RR-active. Various nitrogen sources, such as urea, melamine, ammonia, and polyaniline have been shown to facilitate N-doping of carbon,[11,12] with the doping conditions also being quite versatile, allowing for both *in situ* and post-treatment applications.[13,14]

[a]*Department of Chemistry, University of Calgary, Calgary, Alberta T2N 1N4, Canada. E-mail: birss@ucalgary.ca*

[b]*Department of Chemistry, Alexandria University, Alexandria 21568, Egypt*

[c]*Department of Materials Science and Engineering, University of Toronto, Toronto, Ontario M5S 3E4, Canada*

Nitrogen, with an atomic size similar to that of carbon, integrates well into carbon frameworks, minimizing lattice mismatch. Further, the higher electronegativity of N (3.04) compared to carbon (2.55) facilitates the adsorption of CO_2 on N-C surfaces.[11,12] It is also known that, once N is introduced into the carbon lattice, it can form multiple functionalities, *e.g.*, pyridinic N, pyrrolic N, graphitic N, and oxidized N.[15,16] However, the exact mechanism by which these different N groups influence the CO_2RR when present on N-doped carbon surfaces remains unclear.[13] Challenges therefore include understanding how nitrogen dopants influence the carbon matrix, why different functionalities are reported in different studies, how each of the nitrogen dopants correlate with CO_2RR catalysis, and how to design nitrogen-doped carbon materials that have the optimal combination of N-functionalities to be both highly active and selective towards CO_2 conversion to CO.[17–19]

Another factor that has caused confusion in the CO_2RR/N-C literature is that carbon itself can be highly variable, especially when using high-surface-area carbon powders that are held together with binders, making the mechanistic and kinetic results very difficult to interpret and rigorous comparisons between the results of different CO_2RR studies using carbon substrates challenging. Further, the use of heterogeneous carbon powders with uncontrolled inter-pore dimensions and properties introduces even more uncertainties, compounded by the challenges of characterization and mapping of heterogeneous powders using methods such as electron microscopy, X-ray photoelectron and other spectroscopies. All of these problems have resulted in contradictory and sometimes questionable results in relation to CO_2 activity, durability and selectivity at N-doped carbons, while also showing large variations in the understanding of the factors influencing CO_2RR at N-Cs.[20–24]

In one attempt to simplify carbon structures to better understand the role of N-dopants, highly oriented pyrolytic graphite (HOPG) surfaces were etched through a mask to create ordered pores rich in edge sites, followed by N-doping and then testing for oxygen reduction activity, suggesting that pyridinic N was the most active.[25] In other work, Wang *et al.*[26] reported that a hierarchically structured porous N-doped carbon membrane exhibited high catalytic activity for CO_2RR, with macropores facilitating mass transport, and mesopores and micropores contributing to surface area, enhancing reactant access to active sites. Our team has extensive experience in developing, characterizing and testing carbon materials with tunable and organized nano/microstructures, with the primary goal being to avoid many of the problems discussed above in operating electrochemical devices.

One family of carbons being developed is mesoporous colloid imprinted carbon (CIC) powders, typically formed using mesophase pitch as the carbon precursor and imprinting with silica colloids.[27–33] These carbons have uniform and controllable internal pore size distributions, reproducible pore shapes and neck diameters, controllable surface properties with predictable wettability, ease of surface doping, and an overall highly organized morphology.[30,34] A related self-supported nanoporous carbon scaffold with equivalent and even additional advantages compared to the CIC powders has also been developed and tested.[30,35,36] However, these sheets can be fragile when employed as a support or catalyst to promote gas evolution reactions and thus were not used in the present work.

Here, we focus on the CIC powders, including comparing several methods of N-doping and using rigorous physical characterization of the resulting catalyst properties, then examining them for their CO_2RR activity and selectivity towards CO formation in bicarbonate solutions in an H-cell. This work represents the first time that a series of nano-engineered CICs with controlled internal pore and pore neck sizes, reproducible degrees of carbon crystallinity and defect density, and known N-content and speciation, is prepared and studied to obtain insights into the property/structure/performance relationship of N-carbons for CO_2RR. While the real surface area of these templated carbons is not as high as for many other N-C catalysts, resulting in CO_2RR currents that are in the mid-range of those reported previously, the goal here is primarily to achieve reproducible, controlled and stable physical properties of the carbons and their N-doped counterparts so that interpretation of the results is facilitated.[37–42]

We show first that these mesoporous CICs retain their primary pore size and their exemplary three-dimensional internal interconnectivity after N-doping, even following exposure to high-temperature NH_3, an observation that is essential for the purpose of this study. This has allowed us to deduce that the critical factors yielding the highest selectivity for CO formation at N-C catalysts under our conditions are the pyridinic N content, with these sites exhibiting the highest preference for CO formation *vs.* the HER, as well as a maximal degree of disorder in the carbon walls. To rationalize some of these findings, DFT calculations were carried out, showing that pyridinic- and multi-pyridinic-N sites exhibit the most favourable adsorption strengths for key intermediates, while graphitic and pyrrolic N sites are less active. In addition, the measured CO_2RR kinetics are found to correlate with the total nitrogen content (and hence total pyridinium N content) as well as the accessible surface area. Overall, the best CO_2RR performance was obtained for N-CIC catalysts with a nominal pore size of 12 nm, exhibiting an activity that is comparable to the best-performing N-C catalysts reported so far in the literature.

Experimental methods

Materials

Aniline (≥99.5%, ACS reagent, Sigma-Aldrich), ammonium persulfate (≥98.0%, ACS reagent, Sigma-Aldrich), $KHCO_3$ (GR, Fischer Chemical), NaOH (>85%, ACS reagent, Thermo Scientific), HCl (37%, ACS reagent, Sigma-Aldrich), N_2 (99.999%, Air Liquide ALPHAGAZ 1), Ar (99.999%, Air Liquide ALPHAGAZ 1), NH_3 (>99% anhydrous, Praxair), CO_2 (research grade, Air Liquide), and He (99.999%, Air Liquide) were used as received without further purification. A standard calibration gas (Praxair) containing 5% CO and 20% H_2 (CO_2 balance) was used to calibrate the gas chromatograph.

Mesophase pitch (MP, Momentum Materials Solutions) was used as the carbon precursor, with MP having a softening point of 250 °C, an ash content of <150 ppm, a coking value ≥ 90%,

toluene insoluble of 65 ± 3%, and quinoline insoluble of 42 ± 3%. In terms of the SiO_2 colloids, Nexsil-125-40 (85 nm average particle size), Ludox AS-40 (22 nm), and Ludox HS-40 (12 nm) were used as the templating reagents. Nafion solution (10 wt%, D-10, Fuel Cell Store) in a water/alcohol mixture (45/45 wt%) was used as the ionomer, while either glassy carbon plate (Alfa Aesar, type 1) or carbon paper (CP, AvCarb MGL370, Fuel Cell Store) served as catalyst substrates at the working electrode.

Preparation of colloid-imprinted carbons (CICs) and N-doped CICs (N-CICs)

Colloid-Imprinted Carbon (CIC) powders were prepared using the same silica templating approach previously reported by the Birss group.[31–34,43,44] The samples (Table S1) are referred to as 'CIC-*x*', with *x* being the nominal pore size value, ranging here from 12 to 85 nm. In a typical synthesis, 30 g of dried and ball-milled colloidal silica (having the target particle size) was mixed with 5 g of ball-milled mesophase pitch (MP) powder in 20 mL of butanol. The ball milling step was used under mild conditions only to break up agglomerates formed after drying the silica nanoparticles. The mixture was ball-milled for 2 h at 150 rpm using a programmed milling sequence consisting of 15 min of forward rotation followed by 15 min of reverse rotation, repeated for 7 complete forward–reverse cycles. The resulting slurry was then dried overnight and ground to a fine powder.

The resulting MP–silica composite was thermally treated in a tube furnace (Thermo Scientific Lindberg/Blue M TF55035A-1) under an argon atmosphere. An initial heat treatment was carried out at 400 °C for 2 h to promote silica impregnation, followed by carbonization at 900 °C for 2 h. Both heating and cooling rates were maintained at 5 °C min^{-1}. After carbonization, the silica template was removed by refluxing the composite in 3 M NaOH at 80 °C for 24 h. The solid was then thoroughly washed with deionized water and subjected to a second NaOH treatment in 1 M NaOH at 80 °C overnight in a plastic bottle with occasional stirring. After extensive washing with deionized water, the material was immersed in 0.03 M HCl at 80 °C overnight with occasional stirring. Finally, the product was washed repeatedly with deionized water until the rinse solution was neutral and contained no detectable chloride ions and was then dried in an oven at 80 °C overnight.

All prepared CIC materials were subsequently nitrogen-doped *via* high-temperature ammonia treatment to form N-CIC powders. In a typical procedure, 0.1 g of CIC powder was placed in an alumina boat and inserted into a tube furnace. The sample was heated to 800 °C at a ramp rate of 5 °C min^{-1} under flowing N_2. Once the temperature reached 800 °C, the carrier gas was manually switched from N_2 to pure anhydrous ammonia gas, which was maintained at 800 °C for 7 h. After completion of the ammonia treatment, the gas flow was switched back to N_2, and the furnace was cooled to room temperature at the same rate as used during the heating ramp.

Preparation of aniline-derived carbon powders (AD-22)

Following the literature,[41] the aniline-derived, mesoporous carbon powder, with an expected 22 nm pore diameter (AD-22, Table S1), was prepared as follows. First, 1 mL of colloidal silica suspension (40%, Ludox AS-40, with a nominal particle size of 22 nm) was mixed with 5 mL of 1 M HCl and stirred for 10 min. Subsequently, 0.4 g of aniline monomer was added dropwise to the mixture under continuous stirring. The resulting mixture was then added dropwise, with vigorous stirring, to a solution containing 1 g of ammonium peroxydisulfate (APS) dissolved in 2 mL of 1 M HCl, which was maintained at a low temperature in an ice bath. The combined mixture was stirred for 24 h to allow polymerization to proceed. After this period, the resulting solid was collected by centrifugation, dried, and then pyrolyzed at 1000 °C under a nitrogen atmosphere for 2 h. To remove the SiO_2 template, the carbonized material was treated with 2 M NaOH under stirring and reflux, then filtered and washed until the filtrate was neutral. A second carbonization at 1000 °C under nitrogen atmosphere was conducted for another 2 h, with the final product denoted as AD-22.

Deposition of N-C catalysts on carbon substrates

In the majority of this work, 11.7 mg of N-doped, as-prepared CIC-12/22/85 or AD-22 powder was mixed with 150 μL of 1% Nafion, 250 μL of isopropyl alcohol (IPA) and 1 mL of H_2O to make an ink, which was then sonicated for 30 min. 60 μL of the ink was then drop-casted by pipette onto a pre-polished 1 cm^2 glassy carbon plate and allowed to dry at room temperature. The glassy carbon plate was held in place with a copper clip, which also provided electrical contact to the potentiostat. The ink preparation and deposition procedure used for catalyst stability testing was slightly different from the standard protocol described above. For these tests, the catalyst ink was prepared by dispersing 2.5 mg of catalyst with a mixture of 100 μL isopropanol (IPA) and 50 μL deionized water. 6.5 μL of a 5 wt% Nafion solution was added to the suspension and the mixture was then homogenized. 25 μL of the resulting ink was then drop-cast onto one side of a 1 cm^2 carbon paper (CFP) electrode, while the other side was isolated using wax. The coated CP electrode was subsequently dried on a hot plate at 50 °C for 1 h prior to electrochemical testing. The catalyst loading on both the glassy carbon and carbon fiber paper electrode supports was ~0.5 mg cm^{-2} with ~10 wt% Nafion binder.

Electrochemical measurements and product analysis

A BioLogic SP-300 potentiostat was used to carry out all of the 3-electrode measurements. Cyclic voltammetry (CV) and CO_2 electrolysis at constant potential were performed in a gas-tight glass H-cell with a glass frit used as the separator between the compartment that contained the working electrode (WE) and the Ag/AgCl (3 M KCl) reference electrode, and the second compartment containing the graphite rod counter electrode. To convert the WE potential (E) to the reversible hydrogen electrode (RHE) reference scale, eqn (1) was used, allowing for a correction to be made for the pH difference between N_2-saturated (pH = 8.6) and CO_2-saturated (pH = 7.2) solutions.

$$E(vs.\ \mathrm{RHE}) = E(\mathrm{measured}\ vs.\ \mathrm{Ag/AgCl}) + 0.210\ \mathrm{V} + 0.059\ \mathrm{V} \times \mathrm{pH} \quad (1)$$

Cyclic voltammetry (CV) measurements were carried out in a 0.5 M $KHCO_3$ solution saturated by bubbling Ar or CO_2 for at least 30 minutes, with the solutions in both compartments continuously stirred with a magnetic stir bar. The CO_2RR activity and selectivity of all N-carbon catalysts were evaluated in CO_2-saturated 0.5 M $KHCO_3$ using a gas-tight H-cell.

During chronoamperometric electrolysis, the cell headspace was periodically sampled (50 μL) with a gas-tight syringe (Hamilton 1725) and analyzed using gas chromatography (Agilent 7890B), equipped with a PoraPlot Q and PLOT molecular sieve (5 Å) column (oven temperature 60–120 °C) and a VICI pulse discharge helium ionization detector (PDHID). Helium (99.99%) was used as the carrier gas for CO and H_2 analysis, and retention times were calibrated against standard gases containing known CO and H_2 concentrations. As no liquid products are expected from N-C catalysts, the solution was rarely analyzed after testing.[37–42]

For stability testing, CO_2 purging was stopped, and the potential at which the maximum FE_{CO} was observed was applied to the WE. The current (mA) was recorded as a function of time (chronoamperometry, CA), after which a gas sample was collected from the headspace of the catholyte reservoir for GC analysis. The electrolyte was then re-purged with CO_2 for 30 min before repeating the CA test. These cycles were continued until a noticeable decrease in current was observed or until the end of the constant potential experiment. Long-term stability experiments were conducted under continuous CO_2 flow conditions. During electrolysis, the applied potential was maintained without interruption, and the gaseous CO_2RR products were continuously collected in a 1 L sampling bag. Once the bag was filled, gas analysis was performed by GC every 30 min, after which the bag was exchanged while maintaining uninterrupted electrolysis. This approach ensured continuous operation without potential cycling or pauses during product collection.

Physical characterization methods

The morphology of carbon and N-doped carbon powders studied in this work was determined by field-emission scanning electron microscopy (FESEM, Zeiss Sigma VP) at an accelerating voltage of 4 kV. The samples were attached to double-sided carbon tape attached to an Al SEM sample holder. Energy Dispersive X-ray Spectroscopy (EDS) was carried out using an FEI Quanta 250 FEG environmental FESEM at an accelerating voltage of 15 kV. Transmission Electron Microscopy (TEM) and EDS analysis were conducted using a JEOL JEM-ARM200cF S/TEM, operated at a 200 kV accelerating voltage.

The nitrogen content of the NH_3-doped carbons was determined by X-ray photoelectron spectroscopy (XPS), carried out with a Kratos AXIS Ultra DLD system equipped with an Al source (1486.6 eV). The surface area and pore diameter distribution of all carbon-based samples, before and after N-doping, were evaluated by isothermal N_2 adsorption/desorption at 77 K using a Micromeritics 3Flex instrument. The estimation of the distribution of pores within the materials was achieved by application of the Barrett–Joyner–Halenda (BJH) method to the adsorption data,[30] while a Rigaku Multiflex X-ray diffractometer was used to collect X-ray diffraction (XRD) patterns of the carbon samples. Raman analysis was conducted on a WITec Alpha-300 series confocal Raman microscope, equipped with a diode laser emitting light at a wavelength of 532 nm. The laser power utilized during the measurements was set at 5 mW.

Computational methods

Spin-polarized DFT calculations were performed using the Vienna *Ab initio* Simulation Package (VASP), employing the projector augmented wave (PAW) method and the generalized gradient approximation (GGA) of the Perdew–Burke–Ernzerhof (PBE) functional.[45] van der Waals corrections were accounted for using Grimme's DFT-D3 scheme.[46] A plane-wave energy cutoff of 500 eV was used, with electronic and ionic convergence thresholds set to 10^{-5} eV and 0.02 eV $Å^{-1}$, respectively. Structural optimizations were conducted using a 3 × 3 × 1 Monkhorst–Pack *k*-point grid, and a vacuum layer of 15 Å along the *z*-direction of the graphene structures to prevent interlayer interactions.

The chemical potential of proton–electron pairs was calculated as a function of the applied potential using the computational hydrogen electrode (CHE) model: $\mu(H^+) + \mu(e^-) = \frac{1}{2}\mu(H_{2(g)}) - eU$.[47,48] The free energies for each adsorbate and gas-phase molecule were calculated from: $G = E_{DFT} + E_{ZPE} + \int_0^T C_p dT - TS$, where E_{DFT} is the electronic energy calculated by DFT, E_{ZPE} is the zero-point energy estimated using the harmonic approximation by taking the vibrational frequencies of adsorbates or molecules as calculated within DFT, and $\int_0^T C_p dT$ and TS denotes heat capacity and entropy, respectively. Zero-point energies, heat capacities and entropies were calculated from these vibrations employing standard methods and were then used to convert the electronic energies into free energies at 298.15 K.[49]

Results and discussion

Morphology, pore properties, and crystallinity of CICs, N-doped CICs, and AD-22

Morphological properties from FESEM and TEM imaging. The morphology of the four mesoporous carbons under study here (Table S1), before and after N-doping, was examined using FE-SEM and TEM to both verify successful silica templating and to assess whether exposure to high-temperature NH_3 induces any notable morphological changes in the case of the colloid imprinted carbons (CICs). Representative FE-SEM and TEM images (Fig. 1) show that both the primary pore sizes and the three-dimensional pore interconnectivity within the CICs are essentially the same before and after N-doping by NH_3 treatment at 800 °C, consistent with Table S2. High-resolution TEM (HR-TEM, Fig. 2) imaging further confirms that both the CIC pore diameters and the wall thicknesses between adjacent pores are preserved after NH_3 exposure and subsequent silica removal, which is critical to the overall goals of this work.

As shown in Fig. S1 and summarized in Table S2 (first column), the as-prepared CIC-12 and CIC-22 materials and their N-doped

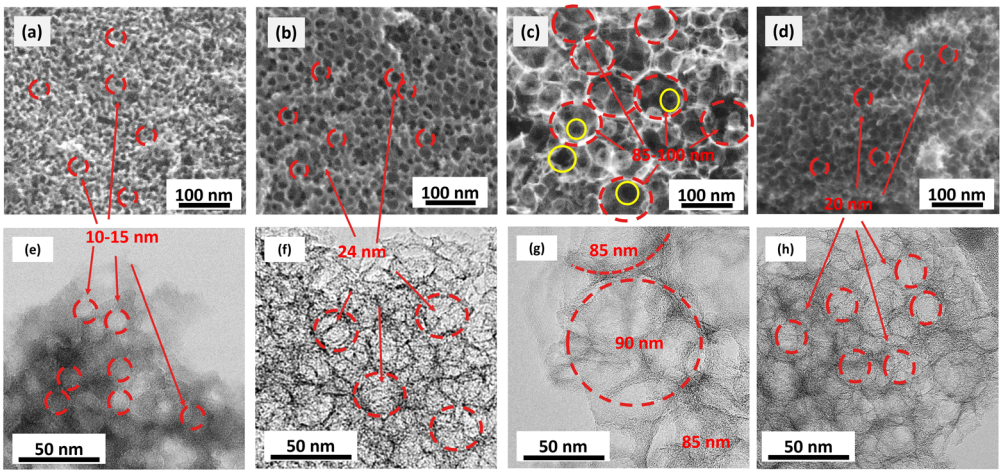

Fig. 1 Representative FESEM images of (a) N-doped CIC-12, (b) N-doped CIC-22, (c) N-doped CIC-85, and (d) aniline-derived AD-22, with (e–h) displaying their corresponding TEM images. The red circles outline the pores, and the red numbers give the associated pore diameters, while the yellow circles in (c) identify the pore necks in CIC-85.

counterparts give average pore diameters that are very similar to the silica colloid size employed. However, in the case of CIC-85, the pore size extends from 85 to 100 nm, arising from a similarly wide size range of the nominally 85 nm silica templating particles.[29] There is also occasional pore wall damage observed for CIC-85 (Fig. S1d and e), further contributing to the slightly larger average pore size than predicted.[32] All of the CIC powders studied here are known to contain interconnected pore networks with approximately twelve pore necks per pore.[30–33] For CIC-85, the ~25 nm pore necks are visible by SEM (Fig. S1e). In contrast, for CICs with smaller primary pore sizes of 12 and 22 nm, the pore necks are not readily resolvable by SEM, because their diameters decrease systematically with decreasing pore size.[31,33]

This work also focuses on a 22 nm silica colloid-imprinted carbon, formed by the thermal decomposition of aniline as both the carbon and nitrogen source and labelled as AD-22. This N-doped material was included in order to directly compare it against the CIC-22 powder, where its carbon was derived from mesophase pitch and subsequently surface N-doped by exposure to high-temperature NH_3. It is seen in Fig. 1d and S1g that AD-22 exhibits similarly uniform but slightly smaller pore sizes than N-CIC-22 (20–22 nm *vs.* 22–24 nm, respectively), while no other significant differences could be discerned, even from the TEM images in Fig. 1h *vs.* 1f, respectively.

Porosity characteristics from N_2 gas sorption. Gas sorption analysis was carried out to confirm the pore sizes and to assess the presence of microporosity within the carbon frameworks, especially within the CICs, as exposure to NH_3 at high temperature is known to etch carbon and generate additional micropores within the carbon walls.[50] Compared with electron microscopy, N_2 sorption probes a much larger quantity of material and therefore provides statistically more representative information about the overall porosity characteristics of the samples. The N_2 adsorption–desorption isotherms collected at 77 K for all samples are shown in Fig. S2. These show that all samples exhibit type IV isotherms, indicating the presence of both mesopores (visible by SEM and TEM) and micropores (not discernible in the microscopy images).

For the smaller-pore-size materials (CIC-12, CIC-22, and AD-22), the hysteresis loops observed at high relative pressures ($P/P_0 > 0.9$) are consistent with H1-type behaviour, indicative of the presence of uniform mesopores.[51] In the lower relative pressure range ($P/P_0 < 0.9$), the hysteresis loops (H3 or H4) are likely indicative of the presence of the smaller pore necks and additional microporosity.[33,43] Although, CIC-85 appears to exhibit characteristics more similar to an H4 isotherm, the absence of slit-like pores in both FE-SEM and TEM images, suggests that its porosity may well fall into the category of an H1 isotherm as well, but with its wider pore size distribution, this may distort the isotherm shape.

Analysis of these results confirms an average pore size of 10–15 nm for CIC-12, 22–24 nm for CIC-22, and around 20–22 nm for AD-22, consistent with the SEM and TEM measurements (Fig. 1 and S1) as well as with former work on the CIC powders by our team.[31,34] Notably, the pore size distribution of CIC-85 and N-doped CIC-85, normally obtained from the adsorption branch, is likely not that useful, as BJH analysis of gas sorption data is not reliable for materials with mesopore sizes larger than ~50 nm.[30] Therefore, the pore size distribution of the CIC-85 and N-doped CIC-85 powders was obtained solely from the SEM and TEM analysis (Fig. 1, 2, and S1).

Another important outcome of the gas sorption analysis (Table S2), which could not be determined from the electron microscopy, is that N-doping of the CICs by exposure to NH_3 at high temperatures leads to a significant increase in the density of micropores within the CIC walls. This increase in microporosity is consistent with NH_3-induced carbon etching and the associated generation of additional defect sites within the carbon framework.

Crystallinity of N-free and N-doped carbon walls. Only a few prior CO_2 reduction studies at N-carbon catalysts have examined the effect of the degree of defectiveness within the carbons

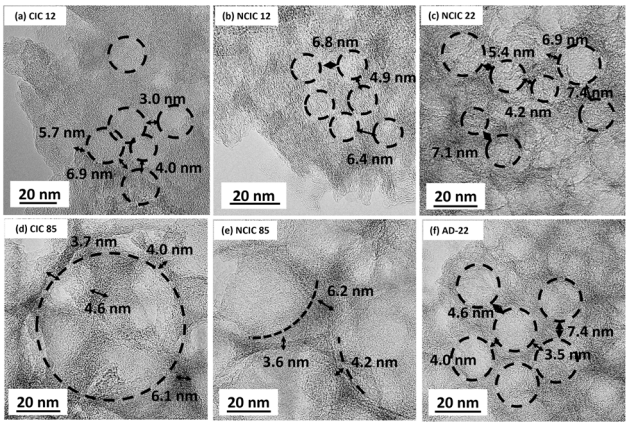

Fig. 2 Representative HR-TEM images (top-down view) of (a) CIC-12, (b) N-CIC-12, (c) N-CIC-22, (d) CIC-85, (e) N-CIC-85, and (f) AD-22 powders, with the black dashed lines outlining the pores and the numbers giving the measured wall thickness between pores at their thinnest points.

themselves and its role, if any, in influencing N content and N speciation after doping. In the CO_2RR literature, Wang *et al.*[52] showed that increasing the intrinsic carbon defect concentration, quantified using Raman I_D/I_G ratios (relative graphitic (G) and disordered (D) carbon content), leads to higher selectivity towards CO formation for both N-doped and undoped porous carbons, while Sharma *et al.*[53] reported that a higher defect density improves CO selectivity in N-doped CNTs. However, to our knowledge, no previous studies have examined carbon-wall crystallinity using XRD-derived metrics, such as the crystallite dimension in the *c*-direction (L_c) or interlayer *d*-spacing (d_{002}), and have also never correlated these structural descriptors with the CO_2RR performance. The combined Raman–XRD analysis used here to evaluate wall defectiveness across the mesophase-pitch-derived CIC family as well as the aniline-generated AD-22 material, therefore represents a unique approach.

The Raman spectra are plotted in Fig. 3a, with the N-doped CIC samples (N-CIC-22, N-CIC-12, and N-CIC-85) showing higher I_D/I_G (peak intensity) ratios compared to their more crystalline undoped counterparts, with a ~13% increase seen for both CIC-12 (1.04 to 1.18) and CIC-85 (1.03 to 1.16), and a 10% increase for CIC-22 (1.00 to 1.10). This confirms that N-doping in high-temperature NH_3 introduces disorder into the mesoporous CIC materials, presumably from a combination of etching, and the generation of more micropores (Table S2). In comparison, AD-22, which was never exposed to an NH_3 environment, exhibits a Raman I_D/I_G ratio of 1.00, close to that of the as-prepared N-free CICs.[40,54] This relatively low ratio and the pronounced G band observed for AD-22 (Fig. 3a) is likely the result of its preparation method, involving polymerization of aniline on a close-packed assembly of silica particles, followed by pyrolysis, a method similar to the techniques used for growing highly ordered graphene on SiO_2 substrates.[55]

The X-ray diffraction (XRD) patterns for CIC-12, CIC-22 and CIC-85, before and after N doping, as well as the pattern for AD-22, are shown in Fig. 3b. Bragg's law and the Scherrer equation were used for the analysis of the graphite (002) peak at $2\theta = 25°$, giving the corresponding interlayer *d*-spacing (d_{002}), with an error of ± 0.005 nm, as well as the crystallite dimension in the *c*-direction (L_c), with an error of ± 0.01 nm, for each sample.[56] The (002) reflection arises from the stacking of graphene layers in graphitic carbon, and therefore the peak broadening provides an estimate of the crystallite stacking height along the *c*-axis (L_c).

It is seen that as-prepared CIC-12 exhibits fairly small crystallite dimensions, similar to commercial carbon black (Vulcan Carbon, VC), which is known to feature an L_c value of ~1 nm, while N-free CIC-22 and CIC-85 have larger L_c values of 1.44 and 1.35, respectively. Most importantly, after N-doping in the NH_3 atmosphere, all N-CICs show a weaker and broader XRD pattern (lower L_c values) compared with their corresponding non-doped counterparts, indicative of the development of a more disordered structure, as also predicted from the Raman spectra (Fig. 3a). In fact, it is known that the introduction of N-containing defects can break and ruffle planar carbon layers, leading to a decrease in microcrystalline dimensions.[57,58] Among the CIC materials, N-CIC-12 exhibits the smallest crystallite dimension (the lowest degree of order) of 0.7 nm, followed by N-CIC-85 at 0.83 nm and AD-22 powder at 0.81 nm. On the other hand, N-CIC-22 shows the least disorder in its walls with a graphene stacking dimension of 1.41 nm.

The unique AD-22 N-C material, synthesized using aniline as both the C and N precursor, exhibits a relatively small L_c value

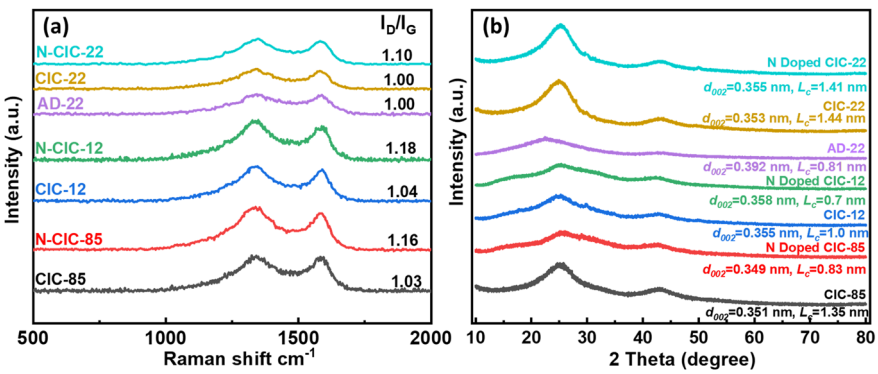

Fig. 3 (a) Raman spectroscopy and (b) XRD patterns of as-prepared CIC-12, CIC-22 and CIC-85, both before and after N-doping, as well as of as-prepared AD-22.

(although still higher than N-CIC-12) and the largest *d*-spacing (Fig. 3b), suggesting the presence of structural disorder. In contrast, its comparatively low I_D/I_G ratio from Raman analysis (Fig. 3a) indicates a higher degree of order within the graphene planes. This apparent discrepancy arises because Raman spectroscopy probes local defects and in-plane order, while XRD reflects the long-range stacking arrangement of carbon layers. Thus, AD-22 likely contains well-ordered, defect-poor graphene sheets that are irregularly stacked, resulting in larger interlayer spacing and smaller crystallite domains overall.

Surface properties of N-free and N-doped mesoporous carbons

STEM/EDX and XPS nitrogen content determination. Partly to verify that N-doping was successful, the presence and distribution of N in the N-C powders was examined by scanning TEM (STEM) equipped with energy dispersive spectroscopy (EDS). For the CICs (Fig. S3–S5), this confirmed that nitrogen (green dots in bottom row) was successfully doped into the surface of the three CICs after NH_3 treatment, as seen from the presence of an N signal in the bottom row, but the absence of a nitrogen signal in the parent non-N-doped CICs (top row). EDS mapping showed that the distribution throughout the CIC networks is highly uniform, with no trace metals or other elements detected. For the AD-22 material, Fig. S6 shows a similarly uniform distribution of nitrogen atoms, as expected from the use of aniline as the starting material.

To quantify the N content, X-ray Photoelectron Spectroscopy (XPS) analysis was carried out on the N-C powder samples, showing distinctly visible nitrogen peaks in the high-resolution N 1s XPS spectra (Fig. 4 and Table S3), with the N 1s peak also clearly observed in the XPS survey spectrum (Fig. S7). Quantitative analysis shows that N-CIC-12 contains 2.3 at% nitrogen, N-CIC-22 gives 1.8 at%, and N-CIC-85 contains 2.5 at% nitrogen (Table S3), with all of the nitrogen dopant located only on the carbon surfaces that were exposed to NH_3. In contrast, AD-22 demonstrated a higher total nitrogen content of 5 at%, likely as nitrogen is present both inside the carbon walls and on the pore surfaces.

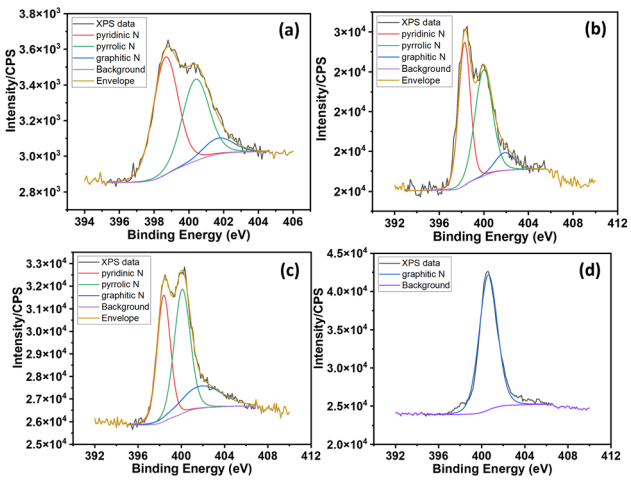

Fig. 4 High-resolution XPS scans of the N 1s region for (a) N-CIC-12, (b) N-CIC-22, (c) N-CIC-85, and (d) AD-22 powders.

N-surface functionalities from XPS. To identify the prevalent nitrogen surface functionalities, the high-resolution N 1s spectra for all N-C catalysts were deconvoluted into three peaks, centred at 398.7, 400.5, and 401 eV, corresponding to pyridinic, pyrrolic, and graphitic nitrogen, respectively (Fig. 4 and Table S3).[15] Further analysis showed that the N-CIC-12 surface is comprised of an average of 53 at% pyridinic nitrogen, 39 at% pyrrolic nitrogen, and 8 at% graphitic nitrogen. In comparison, Table S3 shows that the N-CIC-22 contains a little more pyrrolic nitrogen (48 at%) than pyridinic nitrogen (43 at%) as well as 9 at% graphitic nitrogen, while N-CIC-85 has less pyridinic nitrogen (37 at%) but more pyrrolic (45 at%) and graphitic nitrogen (17 at%).

Uniquely, AD-22 is composed of 100 at% graphitic nitrogen in both its walls and at its surface (Table S3), which aligns with the low I_D/I_G ratio found from the Raman spectral analysis (Fig. 3a). Graphitic nitrogen forms when nitrogen atoms replace carbon atoms within the carbon hexagonal rings, allowing most atoms to remain sp^2-hybridized. This was evident in the Raman spectra with the very large G band for AD-22, indicating that a graphene-like structure predominates in this aniline-derived intrinsically N-doped catalyst. This is likely due to the high-temperature pyrolysis step, together with the *in situ* incorporation of nitrogen from the aniline precursor into the carbon framework, which favours the formation of more thermodynamically stable graphitic nitrogen species.

Surface area of N-free and N-doped carbons from gas sorption data. The gas sorption results (Table S2) show that as-prepared CIC-12, CIC-22 and CIC-85 have surface areas of 440, 260 and 205 $m^2\ g^{-1}$, respectively, consistent with previously reported data.[31] While the SEM images in Fig. 1 and S1 showed no obvious morphological changes after heat-treatment in NH_3 gas, there is a significant increase observed in the surface area of all of these materials, namely ~25% for CIC-12 to 550 $m^2\ g^{-1}$, ~15% for CIC-22 to 295 $m^2\ g^{-1}$, and ~40% for CIC-85 to 406 $m^2\ g^{-1}$. This increase arises from additional microporosity rather than structural collapse. Table S2 shows that the additional area arises primarily from the presence of new micropores after N-doping in high-temperature NH_3, consistent with the expected carbon etching in this medium.[57] Interestingly, AD-22, which was N-doped by the thermal decomposition of aniline, exhibits a surface area of 307 $m^2\ g^{-1}$, a value that is very close to that of as-prepared CIC-22 but is lower than for N-CIC-22, noting that AD-22 never experienced an NH_3 atmosphere during its preparation.

Electrochemically active surface area (ECSA). Another important goal of this work was to confirm if the total internal surface area of the mesoporous N-carbon powders, determined by gas sorption, could be fully wetted and would then be accessible to dissolved CO_2. Here, the ECSA of all N-C catalysts was determined from the double-layer capacitance, measured during cyclic voltammetry (CV) over a potential range where no faradaic electrochemistry can occur, all in CO_2-saturated 0.5 M $KHCO_3$ solution (pH 7.4) (Fig. S8). The ECSA values were then compared to the surface areas obtained from gas sorption studies using Brunauer–Emmett–Teller (BET) theory (Table S2).

For the CIC-based materials, the ECSA of CIC-12 and N-CIC-12 is the highest, at 452 ± 3 m^2 g^{-1} and 518 ± 7 m^2 g^{-1}, respectively, while the ECSA of the CIC-22 and CIC-85 analogues, both in their as-synthesized and N-doped conditions, are significantly lower. This matches the trends (Table S2) from the N_2 physisorption isotherms, noting also that the ECSA of CIC-12 and CIC-85 is in good agreement with prior literature reports for these materials.[31] For AD-22, the ECSA was measured to be 285 m^2 g^{-1}, similar to N-CIC-22, with the values also matching their BET surface areas. Overall, as the ECSA values agree quite closely with their gas-phase surface areas, this argues that full accessibility of the internal porous structure of the N-carbons should be realizable during electrochemical testing in aqueous media.

CO_2 reduction at N-free and N-doped mesoporous carbons

To carry out an initial assessment of the electrochemical activity of the as-prepared and N-doped mesoporous carbon materials towards the CO_2RR, cyclic voltammetry (CV) was conducted first between 0.0 and −1.1 V *vs.* RHE in CO_2-saturated 0.5 M $KHCO_3$ solution (pH 7.2) using a standard 3-electrode glass cell. The solid lines in Fig. 5a show the reduction currents under CO_2 saturation, while the dashed lines were collected under Ar saturation, conditions under which only the hydrogen evolution reaction (HER) can occur. Both N-CIC-12 and N-CIC-85 show a higher current density after CO_2 saturation, giving an early indication of CO_2 reduction (CO_2RR) activity. However, N-CIC-22 shows a similar current under both Ar- and CO_2-saturated conditions, while AD-22 displays a significantly enhanced cathodic current under Ar saturation, indicating a preference for the HER *vs.* the CO_2RR.

However, it should be noted that CVs may not accurately predict the CO_2RR *vs.* HER selectivity or activity. This is because different sites can be active for each specific reaction, and also as the kinetics of the two reactions may be different, even if they occur at the same sites. Therefore, it was necessary to analyze the gaseous products formed at varying potentials to assess catalyst selectivity, noting that no liquid products have been reported to form during CO_2RR at N-doped carbons.[41]

Activity and selectivity of CO_2RR under constant potential

The CO product yield (faradaic efficiency for CO generation, FE_{CO}) during the CO_2RR at the N-doped mesoporous carbons catalysts, mixed with Nafion and deposited on GC substrates, was determined in CO_2-saturated 0.5 M $KHCO_3$ in a gas-tight H-cell. After holding at various potentials *vs.* RHE for times sufficient to accumulate enough product in the working electrode compartment headspace, 50 μL was sampled using a gas-tight syringe and analyzed by gas chromatography (GC), while the current was concurrently monitored with time at each potential.

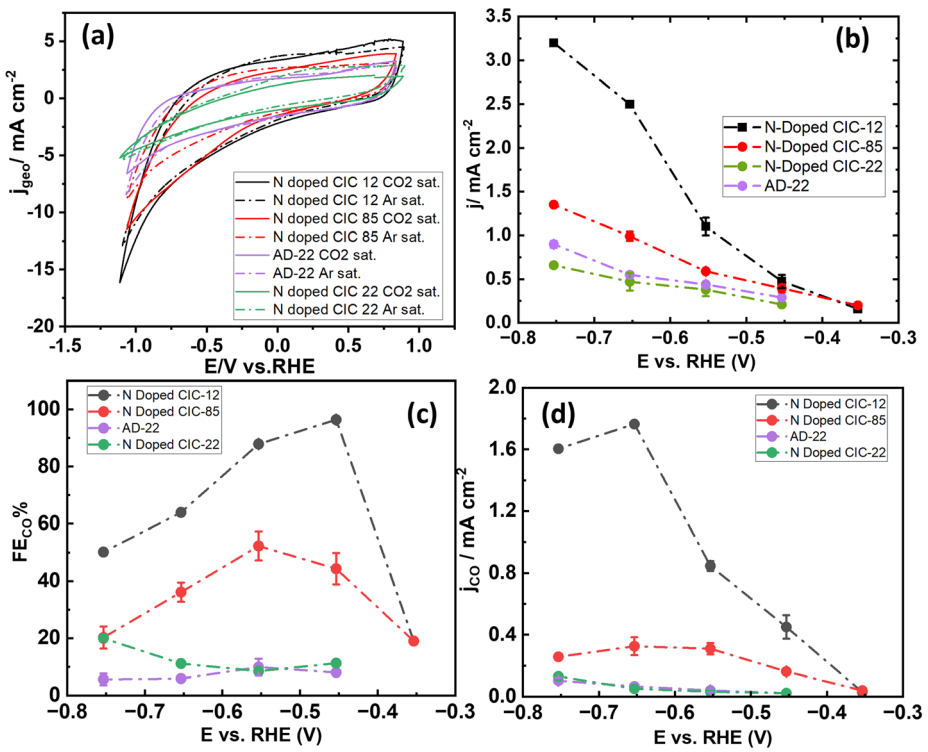

Fig. 5 CO_2 reduction at N-C catalysts in H-cell studies: (a) cyclic voltammetry (50 mV s^{-1}), (b) raw current/potential data showing the steady-state currents at the end of 10 min chronoamperometric experiments, (c) faradaic efficiency of CO formation from GC analysis, and (d) partial currents due only to CO production, all for the N-CIC-12, CIC-22 and CIC-85 powders, as well as AD-22, in CO_2-saturated (solid line) and Ar-saturated (dashed line) 0.5 M $KHCO_3$. In this figure, all current densities were normalized to the geometric surface area and no *iR*-correction was applied. In panel (a), the conventional electrochemical sign convention is used, where cathodic currents are negative, while in panels (b) and (d), the cathodic current densities are plotted in the positive direction for clarity.

Fig. 5b shows the steady-state currents (without *iR* correction) observed at the four N-carbons after roughly 10 minutes at each applied potential, generally showing a weak exponential dependence. While a detailed Tafel analysis was not carried out here, the approximate onset potential is as low as −0.35 V *vs.* RHE (equivalent to an overpotential of ∼0.24 V) for N-CIC-12 and N-CIC-85, but roughly 100 mV more negative (∼0.45 V) for the two N-carbons with 22 nm pore sizes. Consistent with this, the maximum current densities are highest at N-CIC-12, followed by N-CIC-85, but are significantly lower for the 22 nm pore-size catalysts. While the observed current densities are in the mid-range of what has been reported at other N-C powders (Table S4), the real surface area of our mesoporous carbons is also in the low to medium range (Table S2).

In terms of the selectivity of these catalysts towards CO *vs.* H_2 production, N-CIC-12 is clearly the best (Fig. 5c), giving a maximum FE_{CO} of 97% at −0.45 V *vs.* RHE. This is followed by N-CIC-85 at a FE_{CO} of ∼50% at −0.55 V *vs.* RHE, while N-CIC-22 shows a very low FE_{CO} of ∼10% between −0.35 V and −0.55 V *vs.* RHE, then increasing to 20% at −0.6 V *vs.* RHE. This indicates very limited CO_2RR activity at the N-CIC-22 catalysts, while the AD-22 catalyst is essentially CO_2RR inactive.

The partial current attributed to CO formation is shown in Fig. 5d, calculated from the data in Fig. 5b and c. After a period of time of polarization, N-CIC-12 reaches a maximum of 1.8 mA cm^{-2} at −0.65 V *vs.* RHE, followed by N-CIC-85 at a much lower 0.3 mA cm^{-2}, resulting from the combination of both a lower CO selectivity and lower total current (Fig. S9a and b). Both AD-22 and N-CIC-22 show similarly low partial currents for CO formation in Fig. 5d. AD-22 has a low partial current density because of its lower total current density (Fig. S9c) due to its lower surface area and nearly zero FE_{CO}, while N-CIC-22 shows a slightly higher FE_{CO} compared to AD-22 (Fig. S9d).

In terms of the apparent CO_2RR onset potential, Fig. 5c and d show projected values of ∼−0.35 V *vs.* RHE (overpotential of −0.24 V) for both N-CIC-12 and N-CIC-85, and ∼−0.45 V *vs.* RHE (overpotential of −0.34 V) for the 22 nm pore size materials. These values fall within the range reported previously for the most active N-doped carbons (from *ca.* −0.18 V to −0.4/−0.48 V *vs.* RHE; Table S4) and are even better than many, especially all of the more recently reported results (SI, ref. 16–21). The literature comparison summarized in Table S4 also shows that N-CIC-12 achieves one of the highest FE_{CO} values reported for N-doped carbon catalysts in a bicarbonate medium, despite having a relatively moderate BET surface area and nitrogen content as compared to some of the previously reported materials. This highlights the impact of the controlled mesoporous CIC structure in promoting selective CO formation.

Structure–property–performance relationship

Trends in selectivity of mesoporous N-C catalysts towards CO formation. A key goal of this study was to determine the structural, morphological, compositional and N-speciation characteristics of N-doped carbon catalysts that are most influential in generating high selectivity during the reduction of CO_2 to form CO. What makes this objective more achievable in the present work is the use of carbons that have highly reproducible and fully tunable mesopore sizes and shapes, as well as neck diameters, while also having a known carbon wall defect density, N content and N speciation, including after aggressive N-doping by exposure to high-temperature NH_3. This analysis is shown through plots of various physical properties of the catalysts (*y*-axis) *versus* the maximum measured FE_{CO} (*x*-axis) in Fig. 6 for all N-containing carbon catalysts under study here, noting that the maximum FE_{CO} is observed at different potentials for the various catalysts.

Fig. 6a indicates that there is no clear trend between the pyrrolic (red) or graphitic (black) N content and CO selectivity. In contrast, Fig. 6b (black) shows that the pyridinic N functionality is highly correlated with a high CO yield (the distribution (%) of each type of N functionality on each N-C catalyst is given in Table S3). These results indicate that not all carbon defects contribute equally to CO_2RR performance, and that the pyridinic N sites play a key role in determining CO selectivity. In more detail, N-CIC-12 powder exhibits the highest pyridinic N surface content (1.2 at%) and shows the highest maximum FE_{CO} (97%). N-CIC-85 has a somewhat lower pyridinic N content (0.9 at%), resulting in a reduced maximum FE_{CO} of 53%. Although N-CIC-22 possesses a relatively low graphitic N content, its pyridinic N concentration is the lowest among the CIC materials (0.8 at%) and correspondingly exhibits the poorest CO selectivity (FE_{CO} ∼ 20%). This clearly indicates that CO selectivity is governed by the abundance of pyridinic N sites rather than by the graphitic N content. Finally, AD-22 is essentially CO_2RR inactive, ascribed to its close to 100% graphitic N content (0% pyridinic N).

While the identity of the preferred active sites for N-doped carbon is under debate, multiple papers have also suggested that pyridine N species are the most active sites for CO_2 electroreduction to form CO.[15,53,59] Although less commonly reported, N-pyrrolic species have also been identified as active for CO production, noting, however, that most prior studies have involved N-C catalysts with highly variable and uncertain properties, even in a single study, as well as different testing conditions between studies.[22,60,61] Graphitic N has generally been considered poorly active towards CO_2 reduction due to its electrons being in the π* antibonding orbital, making them less available for CO_2 binding.[22,23] However, it has also been suggested that CO_2 reduction does not solely depend on any single type of nitrogen functionality.[39,62] Our results strongly argue that pyridinic surface nitrogen is preferred for CO_2 reduction *vs.* the HER when using structurally controlled N-doped carbon powders that have the same overall morphology, including 3D-interconnected spherical pores, each with 12 necks, and have been N-doped in an identical manner.

To better understand the catalytic role of the nitrogen functionalities in the CO_2RR at N-doped carbons, we used DFT to compute the reaction Gibbs free energies (ΔG) of $*CO_2 \rightarrow *COOH \rightarrow *CO + H_2O \rightarrow * + CO + H_2O$. The electrochemical reduction of CO_2 to CO was examined *via* two key adsorbed intermediates, *COOH and *CO (Fig. 6c), following a widely accepted mechanism proposed for transition-metal and related systems.[63–65] Structural models of graphitic-N (gra-N), pyridinic-

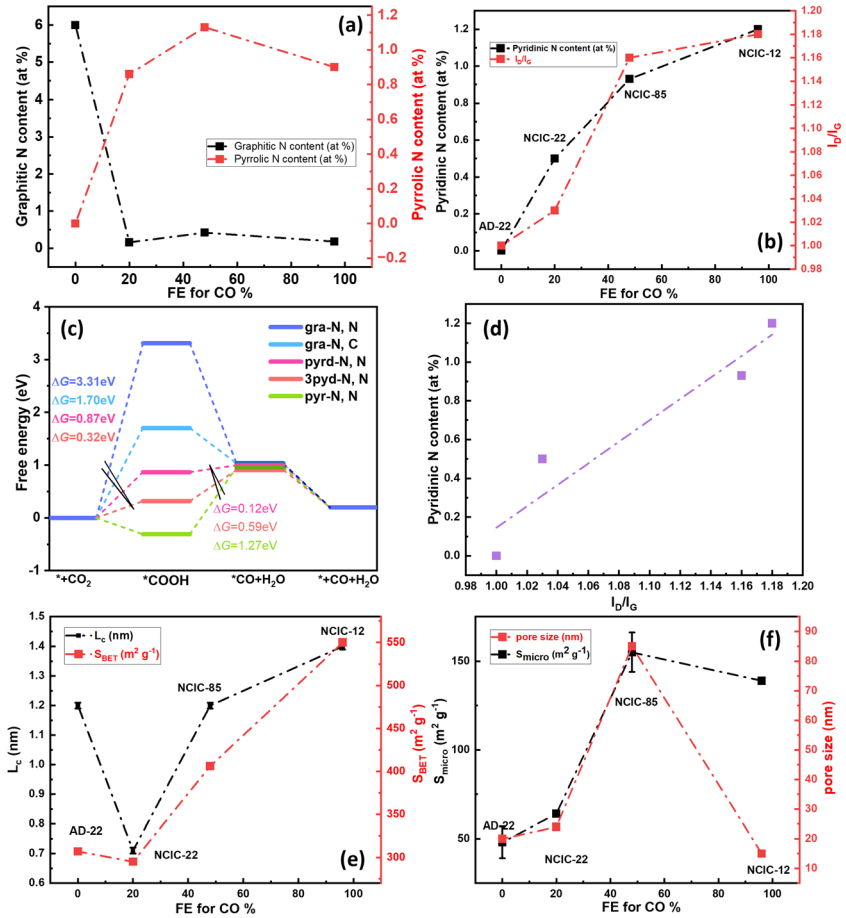

Fig. 6 (a) Maximum FE_{CO} of all N-doped carbons *versus* pyrrolic and graphitic N content from XPS. (b) Maximum FE_{CO} of all N-doped carbons *versus* pyridinic N content from XPS and the I_D/I_G ratio (ratio of defective carbon to graphitic carbon) from Raman spectroscopy. (c) DFT-derived reaction free energy diagram of CO_2RR to CO on surface sites at the N-doped carbon catalysts, with ΔG of the rate-limiting step labelled for each catalyst. (d) Linear relationship of pyridinic N content *vs.* I_D/I_G ratio. (e) The relationship between L_c (crystalline dimension from XRD) and the total micropore BET area *vs.* FE_{CO}, and (f) micropore surface area and pore size *vs.* FE_{CO}, showing no reliable trends. For panels (a), (b), and (d), the nitrogen content (at%) for each N-type (graphitic, pyrrolic, and pyridinic) was calculated by multiplying its XPS percentage by the total nitrogen content from XPS (Table S3).

N (pyd-N), triple-pyridinic-N (3pyd-N), and pyrrolic-N (pyr-N) surface sites were constructed using a 6 × 6 graphene supercell (72 carbon atoms for pristine graphene, Fig. S10). The corresponding free energy diagrams at 0 V *vs.* RHE, obtained based on the computational hydrogen electrode (CHE) model, show that the graphitic-N sites bind the *COOH intermediate too weakly, while pyrrolic-N sites bind *COOH too strongly, both resulting in less favourable energetics to preferentially display CO formation.[47,48] In contrast, the pyridinic-N and triple-pyridinic-N sites show balanced binding strengths, thus promoting the most efficient conversion of CO_2 to CO and giving the highest FE_{CO} values, consistent with our results.

The impact of several other properties of the N-doped carbons on FE_{CO} was also examined, starting with the carbon framework itself, showing that the degree of disorder in the walls of the N-doped mesoporous carbons is highly correlated with FE_{CO} (Fig. 6b). It is clear that the higher the I_D/I_G ratio of the Raman peaks (Fig. 3a) and the higher the degree of disorder within the carbon walls, the larger the FE_{CO} values are, with a plot of the I_D/I_G ratio *vs.* the pyridinic N content showing a linear trend (Fig. 6d). This, in turn, infers that exposure of the CICs to NH_3 at high temperatures causes both the formation of micropores and related wall disorder as a result of the NH_3 etching process, with these then being the sites at which the CO_2RR-active pyridinic N sites preferentially form. For AD-22, as it has negligible pyridinic or pyrrolic N content and is highly ordered, it is found to be CO_2RR-inactive.

In terms of the average crystallite dimension (L_c values) within the walls of the three N-doped CICs, Fig. 6e does show a trend but only if the data for the aniline-derived (AD-22) carbon are excluded. This is reasonable, as L_c and I_D/I_G both change in the same way for the N-CICs, reflecting the common structural origin of wall defectiveness in these materials. Consistent with this, the two catalysts that exhibit the highest FE_{CO} values (N-CIC-12 and N-CIC-85) do have the lowest L_c values. However, the AD-22 material also has a fairly low L_c value and yet generates essentially no CO, likely as its selectivity is fully handicapped by its close to 0% pyridinic N content. Fig. 6e

also reveals that the selectivity towards CO formation increases with the total BET surface area, but only when ignoring the AD-22 data.

Fig. 6f shows that neither the micropore area nor the pore size correlate well with FE_{CO}, not even if the AD-22 catalyst is left out of the analysis. This is somewhat surprising, as if the mouth of the micropores in the carbon walls is where the pyridinic N sites are preferentially formed, a dependence of FE_{CO} on micropore area might have been expected.[53,66,67] However, it is possible that the pyridinic N sites are more prone to form at the pore necks, for example, as pore necks are a unique aspect of the silica-templated carbons studied here. Also, as the pore walls are very thin in these mesoporous materials, consistent with their 90% porosity, the properties of the micropores may be quite different from those that are etched deeply into the typically dense carbon particles used in most previous work.[29,35]

To summarize, it is clear that the most important factors conveying high selectivity towards CO formation at the full set of N-doped mesoporous carbon powders under study here are the type of N functionalities present (pyridinic N is heavily preferred) and a high degree of disorder in the walls of the pores (high I_D/I_G ratio). Having this type of predictive information in terms of which properties lead to high CO selectivity during the CO_2RR should be highly useful for future N-carbon catalyst design.

Trends in activity of mesoporous N-C catalysts towards CO_2 conversion to CO. The currents ascribed to CO formation at the potential at which the highest FE_{CO} was obtained, are plotted on the *x*-axis in Fig. 7 as a function of multiple physical properties of the N-doped carbon catalysts. This shows that the pyridinic N content, shown to give the highest selectivity for CO production, also correlates positively with activity (Fig. 7a), as expected, as the CO_2RR activity should increase the higher the concentration of preferred active sites is present. Another influential factor is the BET surface area, with Fig. 7a showing that the higher the area obtained from gas sorption data or the ECSA (Table S2), the larger the partial current density for CO formation, as expected.

To analyze how heteroatom (N) doping modifies the electronic structure and how this could influence the CO_2RR activity of N-carbon surfaces, DFT was used to calculate the projected density of states (PDOS) of the p_z orbital for the pyridinic and pyrrolic-N sites, as the out-of-plane p_z states constitute the main frontier orbitals interacting with adsorbates at these sites.[68,69] As shown in Fig. 7b, both of the pyridinic-N configurations exhibit a lower density of p_z states near the Fermi level compared to pyrrolic-N, thus weakening the orbital hybridization with *COOH and resulting in a more moderate desorption strength. This balance facilitates both intermediate formation during the CO_2RR, as well as the subsequent conversion steps to form CO, ultimately enhancing the CO_2RR activity. Fig. 7c plots the partial current density for CO formation (*x*-axis) against the graphitic N content and the average mesopore size of the four N-doped carbons, showing no clear trends. As well, Fig. 7d shows that no trends can be seen for the effect of L_c and the micropore area on j_{CO}.

Stability of N-CIC catalyst during CO_2 conversion to CO at N-C in bicarbonate media

In the above work, the CO_2RR performance was measured when steady state was reached over the first 30 minutes of each chronoamperometric experiment. Although not the primary focus of this work, the stability of CO_2RR at the N-doped CIC catalysts (N-

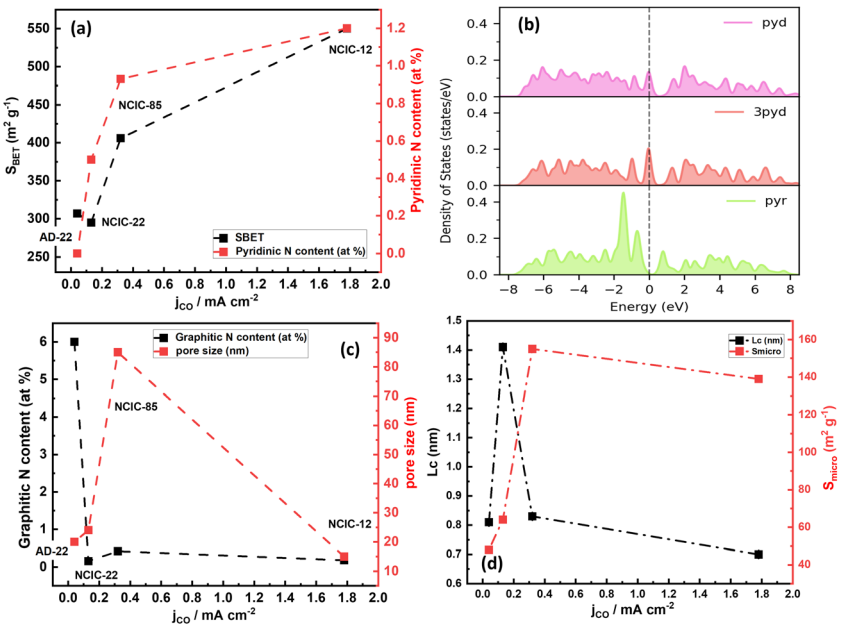

Fig. 7 CO_2RR activity trends – (a) current density at the maximum FE_{CO} during CO_2RR at all N-doped carbons as a function of the pyridinic N content and S_{BET}. (b) Projected density of states within the p_z orbital of pyridinic-N (pyd-N), triple-pyridinic-N (3pyd-N) and pyrrolic-N (pyr-N). (c) Trends of total surface area and pore size of all N-doped carbons and (d) of L_c and micropore of all N-doped carbons surface area, all *vs.* the current density at the potential of maximum FE_{CO}.

C/Nafion ink deposited on carbon paper) was also briefly examined in the H-cell setup using both headspace gas analysis and continuous CO_2 flow methods, as summarized in Fig. S11. Control experiments using bare carbon paper and carbon paper + binder showed negligible CO_2 reduction activity, confirming that the observed activity originates from the N-C catalyst layers.

In the headspace method, chronoamperometry was conducted for 10 min in a quiescent (pre-CO_2-purged) 0.5 M bicarbonate solution (Fig. S11a and b), followed by switching off the applied potential, GC analysis of the headspace gas, followed by 30 min of re-purging before switching on the applied potential again, with each cycle performed at the potential corresponding to the maximum FE_{CO} (from Fig. 5c). As shown in Fig. S11a, the current densities for all three catalysts (N-CIC-12, N-CIC-22, and N-CIC-85) remained almost constant during each 10 min interval and were highly reproducible across three cycles, confirming that the intrinsic activity of the catalysts is stable over short-term testing, even when the potential is periodically switched off/on and CO_2 is alternately bubbled and turned off. However, the FE_{CO} (Fig. S11b) decreased progressively with each cycle, dropping by about 50% for the example of N-CIC-85 after 30 min of total testing, while the current density remained nearly unchanged. This trend suggests that the decline in CO selectivity is not caused by pore blockage or depletion of CO_2 from the cell solution, but more likely the result of either the repeated switching of the potential between open circuit and an applied potential, causing spikes in the current during repeated charge/discharge, or by the switching between active and no CO_2 bubbling.

To test this hypothesis, continuous CO_2 flow experiments were performed using the NH_3-treated mesoporous carbon with an 85 nm pore size (N-CIC-85) as a representative catalyst, with the applied potential never switched off and the outlet gas continuously collected in a Tedlar bag for GC analysis. Under these uninterrupted operating conditions, the current density decreased gradually over the first 90 min, reaching a total loss of about 14% (Fig. S11c). Over the same period, the FE_{CO} decreased modestly from 42% to about 38%, while a about 12% loss in electrochemically active surface area (ECSA) was determined from double-layer capacitance measurements collected before and after the experiment (Fig. S11d). The comparable decreases in current density and ECSA indicate that the dominant degradation mechanism is a gradual loss of electrochemically connected catalyst layer, rather than selective chemical deactivation of specific nitrogen active sites. This interpretation is supported by the visible detachment of small particles of the N-CIC-85/Nafion catalyst layer from the carbon paper substrate during this experiment, likely induced by continuous CO_2 bubbling. In contrast, the smaller relative decrease in FE_{CO} could be due to a combination of factors, including experimental uncertainty in gas quantification and minor changes in the local interfacial environment, as a slight increase in pH near the electrode surface under continuous operation.

Taken together, these results confirm that N-CIC catalysts exhibit stable electrochemical performance over extended operation and that the fairly small apparent current decrease is primarily due to the gradual loss of electrochemically connected area through physical dislodgement rather than loss of intrinsic catalyst activity. This hypothesis is being tested currently in membrane-electrode-assembly experiments, where the CO_2-reducing catalysts are not exposed to solution, and CO_2 is introduced primarily in the gas phase.

Conclusions

This work describes a study of the structure–property–performance of a structurally ordered, highly reproducible family of N-doped mesoporous carbon powders, comparing the selectivity to the formation of CO and the activity of electrochemical CO_2 reduction in aqueous bicarbonate solutions in an H-cell setup. This was facilitated by using internally porous carbon powders, prepared in a controlled manner and possessing tunable (monodisperse) spherical pore and neck sizes with experimentally determined carbon wall defect density, the N content and the percent of each type of N functionality. A series of silica colloid imprinted carbon powders (CIC-*x*), originating from mesophase pitch, was examined, with pore sizes (*x* nm) of 12, 22 and 85 nm. Subsequently, the accessible surface of these carbons was N-doped by exposure to NH_3 at 800 °C. A second type of mesoporous carbon powder was also prepared by pyrolysis of a mixture of aniline and silica particle templates, with pores also 22 nm in diameter, but with nitrogen present intrinsically in both the walls and on the surface of the resulting material.

FE-SEM, TEM, STEM-EDX, and gas sorption analysis showed that the pore diameters and wall thickness remained unchanged after N-doping of the CICs. At the same time, the surface area of the CICs increased significantly after NH_3 exposure, due to the development of micropores as a result of the well-known NH_3 etching process. N-CIC-12 exhibited the highest surface area, followed by N-CIC-85 and N-CIC-22, whereas AD-22 powder, which was never exposed to NH_3, showed the lowest surface area. XRD analysis and Raman spectroscopy revealed structural disorder within the N-doped CIC walls, being most pronounced for N-CIC-12 powder, while XPS analysis showed that the N content of the N-CICs was 1.8–2.5 at%, translating to a ~10% N surface coverage. Although the overall nitrogen content of N-CIC-12 was not the highest, this catalyst exhibited the highest pyridinic N content, while AD-22 showed only graphitic N present.

N-CIC-12 also exhibited the best CO_2 reduction performance, with the lowest onset overpotential and the highest selectivity for CO formation, achieving a faradaic efficiency of 97% at −0.45 V *vs.* RHE. This was followed by N-CIC-85 and then N-CIC-22, while AD-22 was CO_2RR inactive with 100% hydrogen formed. A clear linear correlation was observed between FE_{CO} and both carbon wall defect density and pyridinic-N content, with DFT studies confirming that these sites bind the *COOH intermediate in the most favourable manner, leading to the highest amount of CO produced. The CO_2RR activity also correlated with the nitrogen content as well as the accessible surface area, showing an onset overpotential of only 240 mV at the best catalyst. Both of the pyridinic-N configurations exhibit a lower density of p_z states near the Fermi level compared to pyrrolic-N, thus weakening the orbital hybridization with

*COOH and resulting in a more moderate desorption strength and thus higher rates of CO_2 conversion to form CO.

These insights, taken together, provide highly useful guidance, especially for the design and preparation of new N-doped carbon supports with optimal properties for the catalysis of CO_2 reduction to form CO in aqueous bicarbonate media. Our results should also help guide the selection and preparation of the optimum N-C substrates for the attachment of single metal atom catalysts, as being done by us in parallel work. While not the primary focus of the present work, preliminary stability testing showed that the current density and FE_{CO} can remain stable over long times of testing if the CO_2 flow is continuous and also if the desired potential is applied to the working electrode without any interruptions. More extensive studies are currently underway with a primary focus on testing the N-CIC catalysts in a membrane-electrode assembly configuration.

Author contributions

The manuscript was written through contributions from all authors. All authors have given approval to the final version of the manuscript.

Conflicts of interest

The authors declare no conflict of interest.

Data availability

The data supporting this article have been included as part of the supplementary information (SI). Supplementary information is available. See DOI: https://doi.org/10.1039/d6ta01363e.

Acknowledgements

The authors gratefully acknowledge the financial support provided by the Government of Canada's New Frontiers in Research Fund (NFRF, CANSTOREnergy project NFRFT-2022-00197) for the support of JL, AA, and LH, the Canada First Research Excellence Fund, the Natural Sciences and Engineering Research Council of Canada (NSERC) CREATE ME^2 program for support of JL, and NSERC Discovery Grants awarded to VB and CS. We also acknowledge the Digital Research Alliance of Canada for computing resources for LH and CS, Dr Xuehai Tan at the University of Alberta/Nanofab facility for critical TEM and STEM analyses, Dr Christopher Debuhr from the University of Calgary for SEM imaging, and Dr Rad Sadri (University of Calgary) for his assistance in the evaluation of the XPS and Raman data. We also gratefully acknowledge helpful discussions with Fatemeh Mousavizadeh and Pezhvak Moghaddasisaen, as well as Samantha Luong for help with material synthesis.

References

1 J. Wu, T. Sharifi, Y. Gao, T. Zhang and P. M. Ajayan, *Adv. Mater.*, 2019, **31**, 1804257.
2 W. Ju, A. Bagger, G.-P. Hao, A. S. Varela, I. Sinev, V. Bon, B. Roldan Cuenya, S. Kaskel, J. Rossmeisl and P. Strasser, *Nat. Commun.*, 2017, **8**, 944.
3 H. M. Ansari, P. K. Addo, S. Mulmi, H. Yuan, G. A. Botton, V. Thangadurai and V. I. Birss, *ACS Appl. Mater. Interfaces*, 2022, **14**, 13388–13399.
4 L. D. Ramírez-Valencia, E. Bailon-Garcia, F. Carrasco-Marin and A. F. Perez-Cadenas, *Catalysts*, 2021, **11**, 351.
5 J. Qiao, Y. Liu, F. Hong and J. Zhang, *Chem. Soc. Rev.*, 2014, **43**, 631–675.
6 J. Willkomm, E. Bertin, M. Atwa, J.-B. Lin, V. I. Birss and W. E. Piers, *ACS Appl. Energy Mater.*, 2019, **2**, 2414–2418.
7 J. D. B. Koenig, J. Willkomm, R. Roesler, W. E. Piers and G. C. Welch, *ACS Appl. Energy Mater.*, 2019, **2**, 4022–4026.
8 X. Wang, Q. Zhao, B. Yang, Z. Li, Z. Bo, K. H. Lam, N. M. Adli, L. Lei, Z. Wen, G. Wu and Y. Hou, *J. Mater. Chem. A*, 2019, **7**, 25191–25202.
9 S. Meshitsuka, M. Ichikawa and K. Tamaru, *J. Chem. Soc., Chem. Commun.*, 1974, **5**, 158–159.
10 C. Sun, L. Rotundo, C. Garino, L. Nencini, S. S. Yoon, R. Gobetto and C. Nervi, *ChemPhysChem*, 2017, **18**, 3219–3229.
11 T. Liu, S. Ali, Z. Lian, B. Li and D. S. Su, *J. Mater. Chem. A*, 2017, **5**, 21596–21603.
12 T. Ma, Q. Fan, H. Tao, Z. Han, M. Jia, Y. Gao, W. Ma and Z. Sun, *Nanotechnology*, 2017, **28**, 472001.
13 C. Liu, Y. Wu, J. Fang, K. Yu, H. Li, W. He and C. Chen, *Chin. J. Catal.*, 2022, **43**, 1697–1702.
14 G. An, K. Wang, M. Yang, J. Zhang, H. Zhong, L. Wang and H. Guo, *Molecules*, 2025, **30**, 953.
15 J. Casanovas, J. M. Ricart, J. Rubio, F. Illas and J. M. Jiménez-Mateos, *J. Am. Chem. Soc.*, 1996, **118**, 8071–8076.
16 S. Kundu, T. C. Nagaiah, W. Xia, Y. Wang, S. Van Dommele, J. H. Bitter, M. Santa, G. Grundmeier, M. Bron, W. Schuhmann and M. Muhler, *J. Phys. Chem. C*, 2009, **113**, 14302–14310.
17 P. H. Matter, L. Zhang and U. S. Ozkan, *J. Catal.*, 2006, **239**, 83–96.
18 Y. Shao, S. Zhang, M. H. Engelhard, G. Li, G. Shao, Y. Wang, J. Liu, I. A. Aksay and Y. Lin, *J. Mater. Chem.*, 2010, **20**, 7491–7496.
19 E. J. Biddinger, D. Von Deak and U. S. Ozkan, *Top. Catal.*, 2009, **52**, 1566–1574.
20 Y. Zhu, K. Lv, X. Wang, H. Yang, G. Xiao and Y. Zhu, *J. Mater. Chem. A*, 2019, **7**, 14895–14903.
21 Y. Song, W. Chen, C. Zhao, S. Li, W. Wei and Y. Sun, *Angew. Chem., Int. Ed.*, 2017, **56**, 10840–10844.
22 Y. Song, S. Wang, W. Chen, S. Li, G. Feng, W. Wei and Y. Sun, *ChemSusChem*, 2020, **13**, 293–297.
23 R. Daiyan, W. H. Saputera, H. Masood, J. Leverett, X. Lu and R. Amal, *Adv. Energy Mater.*, 2020, **10**, 1902106.
24 J. Xu, Y. Kan, R. Huang, B. Zhang, B. Wang, K.-H. Wu, Y. Lin, X. Sun, Q. Li, G. Centi and D. Su, *ChemSusChem*, 2016, **9**, 1085–1089.
25 C. Zhang, T. Liu and B. Lu, *Langmuir*, 2025, **41**, 29400–29411.
26 H. Wang, J. Jia, P. Song, Q. Wang, D. Li, S. Min, C. Qian, L. Wang, Y. F. Li, C. Ma, T. Wu, J. Yuan, M. Antonietti and G. A. Ozin, *Angew. Chem.*, 2017, **129**, 7955–7960.

27 B. Pan, C. R. Clarkson, M. Atwa, X. Tong, C. Debuhr, A. Ghanizadeh and V. I. Birss, *Transp. Porous Media*, 2021, **137**, 555–574.
28 B. Pan, M. O. Valappil, R. Rateick, C. R. Clarkson, X. Tong, C. Debuhr, A. Ghanizadeh and V. I. Birss, *Chem. Sci.*, 2023, **14**, 1372–1385.
29 M. Atwa, X. Li, D. O'Connell, R. Sui, R. Marriott and V. I. Birss, *Chem. Mater.*, 2023, **35**, 395–404.
30 M. Atwa, X. Li, Z. Wang, S. Dull, S. Xu, X. Tong, R. Tang, H. Nishihara, F. Prinz and V. I. Birss, *Mater. Horiz.*, 2021, **8**, 2451–2462.
31 F. Forouzandeh, X. Li, D. W. Banham, F. Feng, S. Ye and V. I. Birss, *J. Electrochem. Soc.*, 2018, **165**, F3230.
32 X. Li, D. Banham, F. Feng, F. Forouzandeh, S. Ye, D. Y. Kwok and V. I. Birss, *Carbon*, 2015, **87**, 44–60.
33 X. Li, F. Forouzandeh, T. Fürstenhaupt, D. Banham, F. Feng, S. Ye, D. Y. Kwok and V. I. Birss, *Carbon*, 2018, **127**, 707–717.
34 D. Banham, F. Feng, K. Pei, S. Ye and V. I. Birss, *J. Mater. Chem. A*, 2013, **1**, 2812–2820.
35 M. Atwa, S. Xu, X. Li, S. Dull, Z. Wang, H. Yu, R. Tang, T. Goh, Y. Jung, M. Kiani, M. Lid, H. Nishihara, F. B. Prinz and V. I. Birss, *J. Mater. Chem. A*, 2025, **13**, 33587–33600.
36 J. Li, X. Li, E. El Sawy, S. Maslovara, N. Yasri, V. I. Birss and E. P. L. Roberts, *Mater. Today Commun.*, 2024, **40**, 109773.
37 Y. Shang, Y. Ding, P. Zhang, M. Wang, Y. Jia, Y. Xu, Y. Li, K. Fan and L. Sun, *Chin. J. Catal.*, 2022, **43**, 2405–2413.
38 M. Sevilla, P. Valle-Vigõn and A. B. Fuertes, *Adv. Funct. Mater.*, 2011, **21**, 2781–2787.
39 X. Sun, X. Kang, Q. Zhu, J. Ma, G. Yang, Z. Liu and B. Han, *Chem. Sci.*, 2016, **7**, 2883–2887.
40 P. Yao, Y. Qiu, T. Zhang, P. Su, X. Li and H. Zhang, *ACS Sustain. Chem. Eng.*, 2019, **7**, 5249–5255.
41 G. Wang, Y. Sun, D. Li, H.-W. Liang, R. Dong, X. Feng and K. Müllen, *Angew. Chem.*, 2015, **127**, 15406–15411.
42 P. Lu, Y. Yang, J. Yao, M. Wang, S. Dipazir, M. Yuan, J. Zhang, X. Wang, Z. Xie and G. Zhang, *Appl. Catal., B*, 2019, **241**, 113–119.
43 D. Banham, F. Feng, T. Fürstenhaupt, K. Pei, S. Ye and V. I. Birss, *J. Power Sources*, 2011, **196**, 5438–5445.
44 X. Li, F. Forouzandeh, A. J. Kakanat, F. Feng, D. W. H. Banham, S. Ye, D. Y. Kwok and V. I. Birss, *ACS Appl. Mater. Interfaces*, 2018, **10**, 2130–2142.
45 Y. Ji, Y. Shi, C. Liu and B. Zhang, *Sci. China Mater.*, 2020, **63**, 2351–2357.
46 J. P. Perdew, K. Burke and M. Ernzerhof, *Phys. Rev. Lett.*, 1996, **77**, 3865–3868.
47 S. Grimme, *J. Comput. Chem.*, 2006, **27**, 1787–1799.
48 J. K. Nørskov, J. Rossmeisl, A. Logadottir, L. R. K. J. Lindqvist, J. R. Kitchin, T. Bligaard and H. Jonsson, *J. Phys. Chem. B*, 2004, **108**, 17886–17892.
49 H. A. Hansen, J. B. Varley, A. A. Peterson and J. K. Nørskov, *J. Phys. Chem. Lett.*, 2013, **4**, 388–392.
50 C. L. Mangun, K. R. Benak, J. Economy and K. L. Foster, *Carbon*, 2001, **39**, 1809–1820.
51 M. Thommes, K. Kaneko, A. V. Neimark, J. P. Olivier, F. Rodriguez-Reinoso, J. Rouquerol and K. S. W. Sing, *Pure Appl. Chem.*, 2015, **87**, 1051–1069.
52 W. Wang, L. Shang, G. Chang, C. Yan, R. Shi, Y. Zhao, G. I. N. Waterhouse, D. Yang and T. Zhang, *Adv. Mater.*, 2019, **31**, 1808276.
53 P. P. Sharma, J. Wu, R. M. Yadav, M. Liu, C. J. Wright, C. S. Tiwary, B. I. Yakobson, J. Lou, P. M. Ajayan and X.-D. Zhou, *Angew. Chem.*, 2015, **127**, 13905–13909.
54 P. V. Shanahan, L. Xu, C. Liang, M. Waje, S. Dai and Y. S. Yan, *J. Power Sources*, 2008, **185**, 423–427.
55 S. C. Xu, B. Y. Man, S. Z. Jiang, C. S. Chen, C. Yang, M. Liu, X. G. Gao, Z. C. Sun and C. Zhang, *CrystEngComm*, 2013, **15**, 1840–1844.
56 G. Gupta, D. A. Slanac, P. Kumar, J. D. Wiggins-Camacho, J. Kim, R. Ryoo, K. J. Stevenson and K. P. Johnston, *J. Phys. Chem. C*, 2010, **114**, 10796–10805.
57 H. Li, N. Xiao, M. Hao, X. Song, Y. Wang, Y. Ji, C. Liu, C. Li, Z. Guo, F. Zhang and J. Qiu, *Chem. Eng. J.*, 2018, **351**, 613–621.
58 W. Liu, J. Qi, P. Bai, W. Zhang and L. Xu, *Appl. Catal., B*, 2020, **272**, 118974.
59 F. Li, M. Xue, G. P. Knowles, L. Chen, D. R. MacFarlane and J. Zhang, *Electrochim. Acta*, 2017, **245**, 561–568.
60 Y. Liu, J. Zhao and Q. Cai, *Phys. Chem. Chem. Phys.*, 2016, **18**, 5491–5498.
61 C. Wang, C. Zhu, M. Zhang, Y. Geng and Z. Su, *Adv. Theory Simul.*, 2020, **3**, 2000218.
62 H. Li, N. Xiao, Y. Wang, C. Li, X. Ye, Z. Guo, X. Pan, C. Liu, J. Bai, J. Xiao, X. Zhang, S. Zhao and J. Qiu, *J. Mater. Chem. A*, 2019, **7**, 18852–18860.
63 X. Wang, X. Li, S. Ding, Y. Chen, Y. Liu, M. Fang, G. Xiao and Y. Zhu, *Nano Energy*, 2021, **90**, 106541.
64 Z. Zhang, L. Yu, Y. Tu, R. Chen, L. Wu, J. Zhu and D. Deng, *Cell Rep. Phys. Sci.*, 2020, **1**, 100020.
65 A. Peterson and J. K. Nørskov, *J. Phys. Chem. Lett.*, 2012, **3**, 251–258.
66 J. Wu, M. Liu, P. P. Sharma, R. M. Yadav, L. Ma, Y. Yang, X. Zou, R. Vajtai, B. I. Yakobson, J. Lou and P. M. Ajayan, *Nano Lett.*, 2016, **16**, 466–470.
67 J. Wu, S. Ma, J. Sun, J. I. Gold, C. S. Tiwary, B. Kim, L. Zhu, N. Chopra, R. Vajtai, J. Lou, G. Ding, P. J. A. Kenis and P. M. Ajayan, *Nat. Commun.*, 2016, **7**, 13869.
68 N. T. X. Huynh and V. Chihaia, *Commun. Phys.*, 2022, **32**, 243.
69 O. K. Le and V. Chihaia, *VNUHCM J. Eng. Technol.*, 2023, **6**, 1809–1816.

